

Emission factors and evolution of SO₂ measured from biomass burning in wild and agricultural fires

5 Pamela S. Rickly^{1,2}, Hongyu Guo^{1,3}, Pedro Campuzano-Jost^{1,3}, Jose L. Jimenez^{1,3}, Glenn M. Wolfe⁴, Ryan Bennett⁵, Ilann Bourgeois^{1,2}, John D. Crounse⁶, Jack E. Dibb⁷, Joshua P. DiGangi⁸, Glenn S. Diskin⁸, Maximilian Dollner⁹, Emily M. Gargulinski¹⁶, Samuel R. Hall¹⁰, Hannah S. Halliday¹¹, Thomas F. Hanisco⁴, Reem A. Hannun^{4,12}, Jin Liao^{4,13}, Richard Moore⁸, Benjamin A. Nault¹⁴, John B. Nowak⁸, [Jeff Peischl^{1,2}](#), Claire E. Robinson^{8,15}, Thomas Ryerson^{2,a}, Kevin J. Sanchez⁸, Manuel Schöberl⁹, Amber J. Soja^{8,16}, Jason M. St. Clair^{4,12}, Kenneth L. Thornhill⁸, Kirk Ullmann¹⁰, Paul O. Wennberg^{6,17}, Bernadett Weinzierl⁹, Elizabeth B. Wiggins⁸, Edward L. Winstead⁸, and Andrew W. Rollins²

¹Cooperative Institute for Research in Environmental Science, University of Colorado, Boulder, CO, USA

15 ²Chemical Sciences Laboratory, NOAA, Boulder, CO, USA

³Department of Chemistry, University of Colorado, Boulder, CO, USA

20 ⁴Atmospheric Chemistry and Dynamics Lab, NASA Goddard Space Flight Center, Greenbelt, MD, USA

⁵Bay Area Environmental Research Institute, NASA Ames Research Center, Moffett Field, CA

25 ⁶Division of Geological and Planetary Sciences, California Institute of Technology, Pasadena, CA, USA

⁷Earth System Research Center, University of New Hampshire, Durham, NH, USA

30 ⁸NASA Langley Research Center, Hampton, VA, USA

⁹Faculty of Physics, Aerosol Physics and Environmental Physics, University of Vienna, 1090 Vienna, Austria

35 ¹⁰Atmospheric Chemistry Observations and Modeling Laboratory, National Center for Atmospheric Research, Boulder, CO, USA

¹¹Environmental Protection Agency, Research Triangle, NC, USA

40 ¹²Joint Center for Earth Systems Technology, University of Maryland Baltimore County, Baltimore, MD 21250, USA

¹³Goddard Earth Science Technology and Research (GESTAR) II, University of Maryland Baltimore County, Baltimore, MD, USA

45 ¹⁴CACC, Aerodyne Research, Inc.

¹⁵Science Systems and Applications, Inc., Hampton, VA, USA

50 ¹⁶National Institute of Aerospace, Resident at NASA Langley Research Center, Hampton, VA, USA

¹⁷Division of Engineering and Applied Science, California Institute of Technology, Pasadena, CA, USA

^anow at: Scientific Aviation, Boulder, CO, USA

55 *Correspondence to:* Pamela S. Rickly (pamela.rickly@noaa.gov) and Andrew W. Rollins (andrew.rollins@noaa.gov)

60 **Abstract.** Fires emit sufficient sulfur to affect local and regional air quality and climate. This study analyzes SO₂ emission factors and variability in smoke plumes from U.S. wild and agricultural fires, and their relationship to sulfate and hydroxymethanesulfonate (HMS) formation. Observed SO₂ emission factors for various fuel types show good agreement with the latest reviews of biomass burning emission factors, producing an emission factor range of 0.47 – 1.2 g SO₂ kg⁻¹ C_v. These emission factors vary with geographic location in a way that suggests that deposition of coal burning emissions and application of sulfur-containing fertilizers likely play a role in the larger observed values, which are primarily associated with agricultural burning. A 0-D box model generally reproduces the observed trends of SO₂ and total sulfate (inorganic + organic) in aging wildfire plumes. In many cases, modeled HMS is consistent with the observed organosulfur concentrations. However, a comparison of observed organosulfur and modeled HMS suggests that multiple organosulfur compounds are likely responsible for the observations, but that the chemistry of these compounds yield similar production and loss rates to that of HMS, resulting in good agreement with the modeled results. We provide suggestions for constraining the organosulfur compounds observed during these flights and we show that the chemistry of HMS can allow for organosulfur to act as a S(IV) reservoir under conditions of pH > 6 and liquid water content > 10⁻⁷ g sm⁻³. This can facilitate long-range transport of sulfur emissions resulting in increased SO₂ and eventually sulfate in transported smoke.

Deleted: in the emissions

Deleted: increased

Deleted: (

Deleted:)

Deleted: (> 10⁻⁷

Deleted: (

Deleted: > 10⁻⁷

Deleted:)

Formatted: Superscript

Deleted: /m³

Deleted: /

1 Introduction

80 Sulfate is a major component of PM_{2.5}, contributing significantly to adverse air quality and severe haze events (Chan and Yao, 2008). A severe haze event in Beijing, China showed PM_{2.5} sulfur concentrations reaching 100 µg m⁻³ with aerosol optical depths over 1 (Moch et al., 2018). Sulfate aerosols are produced through the oxidation of sulfur dioxide (SO₂) which was estimated to have a global emission rate of approximately 113 Tg S yr⁻¹ in 2014 (Hoesly et al., 2018). Approximately 67% of global SO₂ emissions are due to anthropogenic sources, primarily fossil fuel combustion and smelting (Lee et al., 2011; Smith et al., 2011; Feinberg et al., 2019).

85 While biomass burning is expected to contribute a smaller portion to global sulfur emissions (1.22 Tg S yr⁻¹), the effects of climate change and land use change are expected to increase biomass burning events in both frequency and duration (Westerling et al., 2006;

100 Heyerdahl et al., 2002; Lee et al., 2011). Biomass burning SO₂ emissions can influence air quality through sulfate aerosol production in regions thousands of kilometers away from the burn site due to meteorological long-range transport (Fiedler et al., 2011). In extreme cases, pyrocumulonimbus formation injects biomass burning aerosol – including sulfate – into the upper troposphere and lower stratosphere (Fromm et al., 2005).

105 Biomass burning produces both primary and secondary aerosols, with sulfate aerosols resulting mostly from secondary production, but with a smaller primary component in some cases (Lewis et al., 2009). The chemical composition of aerosols produced during biomass burning is highly dependent on the environmental conditions and type of combustion occurring, flaming or smoldering. For example, elemental carbon and NO_x are mainly emitted during the flaming stage, while emissions of VOCs and (mainly organic) PM_{2.5} are larger during the smoldering phase (Pandis et al., 1995; Lobert et al., 1991; Burling et al., 2010). Fuel composition also influences SO₂ emissions. This is demonstrated in a recently published compilation of biomass burning emission factors utilizing only data from young smoke to limit conversion during chemical aging, reducing the variability within the published measurements (Andreae, 2019). This compilation shows savanna and grassland SO₂ emission factors to be 0.47 ± 0.44 SO₂ kg⁻¹ C and those for agricultural residues to be 0.80 ± 0.71 g SO₂ kg⁻¹ C with a full fuel type range of 0.2 to 0.87 g SO₂ kg⁻¹ C.

110 Oxidation of SO₂ in both the gas and aqueous phase produces sulfate, with a typical SO₂ lifetime of 0.6 – 2.6 days (Pham et al., 1995; Koch et al., 1999). However, the importance of some conversion mechanisms of SO₂ to sulfate remains poorly understood, resulting in the frequent underprediction of sulfate concentrations by up to a factor of two for regional atmospheric models (Wang et al., 2016; Shao et al., 2019; Wang et al., 2014). This underprediction has been reported for industrialized pollution where limited photochemistry is observed as a result of aerosol dimming (Cheng et al., 2016; Shao et al., 2019). While no known studies have reported on the modeling of SO₂ and sulfate chemistry in biomass burning smoke plumes, it is possible that similar phenomenon could occur because biomass burning plumes can have very high aerosol loading and thus dimming. However, the chemistry is likely to be different as a result of differing emissions. In addition, it has been suggested that unaccounted-for hydroxymethanesulfonate (HMS) formation may explain the discrepancy between measured and modeled sulfate values (Dovrou et al., 2019; Song et al., 2021).

125 In this study, we quantify SO₂ emissions and examine the production of sulfate using airborne observations within a variety of smoke plumes. These measurements provide insight into the variable emission factors observed during biomass burning and allow for a comprehensive analysis of the conversion of SO₂ to sulfate and HMS including both gas- and aqueous-phase conditions. Smoke is a highly dynamic environment, and we examine how sulfur chemistry is affected by radiation attenuation, enhanced aerosol liquid water content (LWC), and variable pH.

2 Methods

140 2.1 Mission and measurements

FIREX-AQ was a joint NASA-NOAA mission to study multiple aspects of fire emissions, chemistry, and impacts. Here we utilize observations from the NASA DC-8. The base locations for this aircraft campaign were Boise, ID, from 21 July to 17 August and Salina, KS, from 18

Deleted: also

Deleted: g

Deleted: in atmospheric models

Deleted: S

August to 5 September, 2019. The Boise location allowed for the measurement of western U.S. wildfires, with sampling occurring in the late afternoon through evening. Salina-based flights focused on prescribed burns, primarily of croplands, within the midwestern and southern regions of the U.S. with measurements typically occurring in the afternoon. A subset of these measurements including seven different fuel types from over 80 fires is reported here.

Flight paths differed between the wildfire and cropland measurements. A typical flight path through the wildfire smoke plumes consisted of two “lawnmower” patterned passes consisting of about 10 staggered downwind transects perpendicular to the plume (Fig. 1). The closest transects were generally 10–15 km downwind due to flight restrictions, with the pattern extending as far as 200 km downwind, resulting in smoke ages (based on Lagrangian trajectory analysis) ranging from tens of minutes to several hours. In contrast, sampling of smaller agricultural fires typically involved 1–2 plume transects per fire.

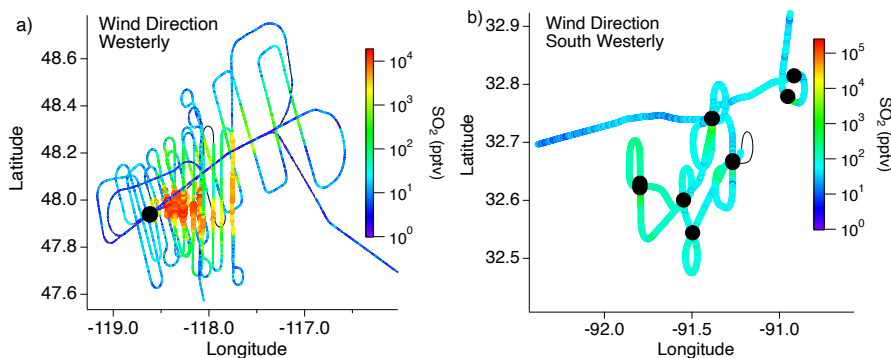


Figure 1. Typical flight path through (a) wildfire and (b) agricultural fire smoke plumes with the color and size of the markers indicating the SO_2 mixing ratio and the black markers indicating the fire locations.

In situ measurements of SO_2 were performed using laser induced fluorescence (LIF SO_2) in which SO_2 was excited at 216.9 nm by a custom-built fiber laser system with the red-shifted fluorescence detected between 240 and 400 nm. An intercomparison performed between the LIF SO_2 and Caltech CIMS instrument during FIREX-AQ showed good agreement between the two measurement techniques (Rickly et al., 2021). The accuracy of the LIF SO_2 measurements is $\pm 9\% + 2 \text{ pptv}$, primarily dictated by uncertainty in the calibration standard concentration and spectroscopic background.

Sulfate measurements were performed with an Aerodyne high-resolution time-of-flight aerosol mass spectrometer (AMS) (DeCarlo et al., 2006; Canagaratna et al., 2007). This measurement technique allows for the speciation of submicron non-refractory particulate mass and the direct separation of inorganic and organic species having the same nominal mass to charge ratio (DeCarlo et al., 2006; Canagaratna et al., 2007). The standard AMS data analysis software reports both inorganic and organic sulfate as total sulfate, complicating the quantification of both types of sulfates (Farmer et al., 2010). While in the case of AMS total nitrate, techniques for rapid assignment of organic nitrate based on its fragmentation pattern have been successfully developed (Fry et al., 2013; Day et al., 2021), the sulfate fragmentation pattern

Deleted: , ID

Deleted: -

Deleted: 10's

Deleted: -

Deleted: intersections

Deleted:

Deleted: $\pm 9\% + 2 \text{ pptv}$

190 is much more variable and hence similar approaches have so far had mixed success, depending
 on the aerosol characteristics (see Schueneman et al., 2021 for a review). In this work, we found
 on the ion fragmentation method to produce reasonable results, based on the consistency with the
 results using positive matrix factorization (PMF, Paatero et al., 1994, Ulbrich et al., 2009) and
 195 the measurements of submicron sulfate aerosol by the mist chamber/ion chromatograph (MC/IC)
of the soluble acidic gases and aerosol (SAGA) instrument, which quantifies only inorganic
sulfate. Both MC/IC and AMS sample submicron particles (van Donkelaar et al., 2008; Guo et
al., 2021). The correlation between the AMS inorganic sulfate and MC/IC sulfate shows an
 overall good agreement (Fig. S8), which adds confidence to the AMS apportionment. However,
 as discussed in section 4.2.2, for certain types of organosulfur compounds, hydrolysis in the
 liquid phase after capture into the instrument and before analysis might lead to MC/IC detecting
 200 these as well, hence a larger uncertainty may be reflected by the MC/IC sulfate measurements
based on the default accuracy estimates for this instrument for inorganic sulfate under FIREX-
AQ conditions (Dibb et al., 2002; Scheuer et al., 2003).

In situ CO concentrations were measured via wavelength modulation spectroscopy
 205 (Sachse et al., 1991), with an uncertainty of 2–7% over the dynamic range of the measurements.
 In situ CO₂ concentrations were measured using non-dispersive infrared spectrometry using a
 modified commercial spectrometer (Model 7000, LI-COR) similar to Vay et al. (2009), with
 uncertainties varying between 0.25 ppm and 2% of the measurements (whichever is larger) over
 the range of the measurements.

2.2 Emission factor calculation

Emission factors (EF) are defined as the mass of compound X relative to the mass of fuel
 burned; however, this can be substituted with the mass balance method which approximates the
 215 fuel mass by the sum of emitted carbon (Andreae, 2019). In accordance, the emission factors for
 SO₂ and sulfate were calculated as the enhancement ratio of each compound relative to the
 enhancement ratio of total carbon emitted per fire in units of g kg⁻¹ (Eq. 3.1). Because CO and
 CO₂ comprise approximately 95% of total carbon emissions, the summation of these values was
 used to represent total carbon.

$$220 \quad EF(X) = \frac{X}{CO+CO_2} \cdot \frac{MM_X}{MM_C} \cdot F_C \cdot 1000 \quad (3.1)$$

The orthogonal distance regression slope of compound X to total carbon ($\frac{X}{CO+CO_2}$) was
 225 determined for each transect through the smoke plume with a smoke age < 1 hr to limit the
 influence of chemical processing due to atmospheric aging. Only emission ratio values with R² >
 0.5 were included in the EF analysis. It is shown in sections 3.3 and 3.7 that no significant aging
 of SO₂ occurs within this length of time. In addition, only measurements ≥ 25% enhanced from
 the background were used, which allowed for the background mixing ratios to be neglected.
 230 MM_X and MM_C represent the molar mass of compound X and the summation of CO and CO₂,
 respectively. The approximated value of 45% is used to represent the carbon fraction (F_C) of the
 fuel emitted during these biomass burning events as outlined by Susott et al. (1996) and allows
 for a more direct comparison to the compilation of EF data prepared by Andreae (2019).

2.3 Modified combustion efficiency

Deleted: , and a measurement of S(IV) the inorganic

Deleted: sulfate speciation provided

Deleted: . As an additional constraint, the AMS apportionment can be compared with ion chromatography the submicron sulfate MC/IC measurements reported by the SAGA instrument (Dibb et al., 2002; Heim et al., 2020), which quantifies only inorganic sulfate.

Deleted: apportionment

Deleted: SAGA measurements of

Deleted: inorganic

Deleted: S8).

Deleted: SAGA

Deleted: SAGA

Deleted: can be considered an

Deleted: upper limit on

Deleted:

Deleted: -

Deleted: ,

Deleted: 3

Deleted: 4

255

The modified combustion efficiency (MCE) is a metric for combustion stage. The MCE is defined as the enhancement of CO₂ from the background in relation to the summation of the enhanced CO and CO₂ mixing ratios (Eq. 3.2). Traditionally, MCE > 0.9 is indicative of the flaming stage and an MCE < 0.9 is representative of the smoldering stage (Ferek et al., 1998; Sinha et al., 2003; Zhang et al. 2018). In reality, smoke sampled from large wildfires likely reflects a combination of variable fractions of flaming and smoldering combustion.

260

$$MCE = \frac{CO_2}{CO+CO_2} \quad (3.2)$$

265

2.4 Box Model

Deleted: 5

The Framework for 0-D Atmospheric Modeling (F0AM, Wolfe et al., 2016) was used to evaluate the evolution of SO₂ downwind of the fire location (Wolfe et al., 2016). Within F0AM, the Master Chemical Mechanism (MCM) version 3.3.1 was used to describe the evolution and chemistry of the gas-phase SO₂ and oxidant species. An additional mechanism describing the conversion of SO₂ to sulfate was implemented to address aerosol oxidation processes of sulfur compounds based on an establishment of equilibrium of the S(IV) compounds and oxidant species with relation to pH (Tang et al., 2014; D’Ambro et al., 2016; Seinfeld and Pandis, 2006).

270

275

A complete list of the aqueous phase reactions and measurements used for model input is included in Tables S1 & S2 and the mechanism code is provided in the Supplementary Section 2.

Deleted: -2

The model was implemented to investigate the chemistry that occurred during the Williams Flats fire which started 2 August 2019 by lightning ignition of timber/slash fuels in Keller, WA. Two separate flight days, 3 and 7 August, were modeled here using measurements acquired by the DC-8 in which two passes of lawnmower patterns were completed. These flights were analyzed by applying a Lagrangian model approach. The measurements were corrected for dilution by normalizing to CO (Müller et al., 2016) as follows:

280

Deleted: -

Deleted: was

Deleted: through

Deleted: pattern

Deleted: paths

$$\Delta_{dil}X = \frac{(X-X_b)}{(CO-CO_b)} \cdot CO_i \quad (3.3)$$

285

in which $\frac{X}{CO}$ represents the ratio of compound X at each transect with respect to CO, X_b and CO_b are the background concentrations, and CO_i represents the carbon monoxide mixing ratio at the source of the fire determined from the extrapolation of the transect average CO values. This extrapolation method was also applied to the dilution-normalized mixing ratios in order to initialize the model back to the fire source (t=0). The model was constrained to these initial concentrations, then allowed to run freely through the remainder of the flight time. The dilution rate was determined by matching the modeled CO to the measured CO decay using a Gaussian fit. However, CO_i used to determine the dilution-normalized mixing ratio values, was based on the extrapolated CO initial value based on all transect CO values (core and edge).

Deleted: dilution

295

Measurements were acquired through aircraft smoke plume penetration, which provided pseudo-Lagrangian observations by not entirely following the same air parcel. Comparison to a Lagrangian simulation is challenging because the aircraft measured different parts of the plume (core vs. edge) and at different emission times. As a result, an exponential fit applied to the SO₂ and sulfate dilution-normalized mixing ratios against plume age is used to represent the

measurement trend for comparison to the model results. While the model is not expected to precisely reproduce the measurements based on plume age, due to variations in altitude between transects and subsequently varied pressures and temperatures, it does allow for the comparison of the overall trends of SO₂ and sulfate downwind of the source using averaged meteorological constraints.

Uptake of SO₂ and the oxidant species (O₃, NO₂, H₂O₂, and HCHO) to aerosol was represented within the model mechanism as a first-order loss (Seinfeld and Pandis, 2006):

$$k_{het} = 0.25 \cdot \gamma \cdot c \cdot v \quad (3.4)$$

where γ represents the uptake coefficient, c is the mean molecular speed of SO₂, and v is the aerosol surface area based on average dry particle size distributions measured by a Laser Aerosol Spectrometer 3340. To account for the gas-phase diffusion limitation, γ was calculated by the following equation:

$$\gamma = \frac{1}{\alpha} + \frac{0.75 + 0.286Kn^{-1}}{Kn \cdot (Kn + 1)} \quad (3.5)$$

where α represents the mass accommodation coefficient and Kn is the Knudsen number. Mass accommodation and gas diffusion coefficients used for deriving Kn and γ are listed in Table S3.

To represent equilibrium partitioning between the gas and aqueous phases, rates of condensation and evaporation were applied as described by D'Ambro et al. (2016):

$$k_{cond} = k_{het} \quad (3.6)$$

$$k_{evap} = \frac{k_{het}}{H \cdot LWC} \quad (3.7)$$

where H represents the Henry's Law constant of the species being adsorbed and LWC is the liquid water content of the cloud or aerosol. The dry particle size (not ambient particle size) is incorporated into k_{het} through Eq. 3.4. This k_{het} value is then applied to Eq. 3.7 as a ratio to the LWC and ability of uptake (H), allowing for calculation of the gas-particle equilibrium. Therefore, as the particle size increases, greater condensation is able to occur, but this also allows for increased evaporation. However, with an increase in LWC and H , less evaporation will be expected. Using this method of uptake and evaporation does not allow for equilibrium of all processes to be assumed as is done in the ISORROPIA calculations. Because S(IV) production is pH dependent, individual equilibrium constants in relation to the H⁺ produced by each reaction are required as an additional factor in the k_{evap} denominator as described by Seinfeld and Pandis (2006). As a result, the model accurately reproduces the S(IV) pH dependence (Fig. S1a) in which HSO₃⁻ is the dominant form between the pH range of 2-7 and SO₃²⁻ becomes the dominant form at pH > 7. Table S1 lists all aqueous phase reactions.

The rate of S(IV) oxidation exhibits a pH dependence based on the available oxidant species (Table S1) (Cheng et al., 2016). Using our model and the initial conditions from Guo et al. (2017), we reproduced very similar pH dependent oxidation rates to those shown in that study. However, initializing the model with the higher concentrations observed during FIREX-AQ increases the rates of oxidation as shown in Fig. S1b. This results in S(IV) oxidation being dominated by reaction with hydrogen peroxide at pH values < 5 which is within the range that aerosol sulfate production most commonly occurs in the U.S. For pH values approaching 5, there

Deleted: ,

Deleted: it does

Deleted: -

355 may be some competition amongst H₂O₂, O₃, and HCHO depending on the oxidant
concentrations. As pH values increase above 5, O₃, NO₂, and HCHO become the dominant
oxidants with H₂O₂ and NO₂ oxidation declining rapidly. Although the reaction of HCHO with
S(IV) results in HMS production rather than inorganic sulfate, it has been included here to
demonstrate its impact on S(IV) oxidation. HCHO adduct formation follows a very similar trend
to O₃ oxidation, becoming a major S(IV) reactant at higher pH. Further discussion of the HMS
reactions listed in Table S1 can be found in the supplement.

360 In this study, aerosol LWC and pH were determined via ISORROPIA-II thermodynamic
modeling (Fountoukis and Nenes, 2007) in forward mode based on the AMS measured aerosol
composition (SO₄, NO₃, NH₄, Cl) and collocated gas-phase measurements of NH₃ and HNO₃
from PTR-MS and CIMS, respectively. NH₃-NH₄ is the most important species pair for
constraining pH because it was not completely in either the gas or particle phase in the fire
plumes or the background air mass. To improve the accuracy in thermodynamic modeling
365 predictions, we removed the outliers when the predicted particle phase fraction of the NH₃-NH₄
partitioning is off by $\geq 40\%$ compared to the observation (4.6% of the data). The gas-particle
partitioning is reproduced with ISORROPIA-II, with the regression slopes of predicted NH₃,
NH₄, and NO₃ close to one compared to the observations and highly correlated (slopes: 0.949,
1.116, and 1.002; r^2 : 0.991, 0.96, and 0.99996, respectively). This also supports the assumption
370 of equilibrium, as the characteristic time for fine particle water equilibrium is very short (< 1 s)
(Pilinis et al., 1989) and ranges from 20 mins or less (Dassios and Pandis, 1999; Cruz et al.,
2000; Fountoukis et al., 2009; Guo et al., 2018) up to 10 hrs for semivolatile components, NH₃,
HNO₃, and HCl (Meng and Seinfeld, 1996; Fridlind and Jacobson, 2000; Shingler et al., 2016).
The uncertainty in particle pH is estimated to be within 0.5-1 unit based on the sensitivity of pH
375 to NH₃-NH₄ partitioning and varies from point to point depending on the model reproduction of
the partitioning (Guo et al., 2017). Because these calculations are based on the inorganic aerosol
concentrations, the LWC could potentially be up to several times greater due to the dominant
organic portion in the fire plumes despite the lower hygroscopicity compared to the inorganics
(Kreidenweis et al., 2008; Guo et al., 2015; Brock et al., 2016). The mixing state of inorganic and
380 organic for the particles in the early phase plumes remains to be investigated but is likely to be
phase separated given the low oxidation state of the organics (Sullivan et al., 2020). The current
modeling can be interpreted as assuming a phase separation of inorganic vs. organics, with the
chemistry studied occurring only in the inorganic-dominated phase and its associated water, with
no kinetic limitations due to potential core/shell or micelle-like structures present in the particles.
385 Propagating the uncertainties of AMS inorganics (34%) and DC-8 total water measurement (3%
based on the observed RH) gives an LWC uncertainty of 39% (Guo et al., 2015). Due to the
dominant organic fraction of sulfate signals in the fire plumes investigated in this study,
additional bias and uncertainty derive from using the total AMS SO₄ signals and zero non-
volatile cations (e.g., not accounting for the potential contribution of soluble ions from ash,
390 Adachi et al, 2022) in estimating LWC and pH. This is of particular concern when the
uncertainties are larger than the estimated free acidity based on ion balance, as often happens
near the neutralization point, The potential bias is estimated to be -0.96±0.95 unit for pH (i.e.,
biased low).

395 Most importantly, the modeling work presented in this study assumes an ideal solution.
Given the relatively high ionic strength conditions observed for the 3 Aug (89.5 ± 19.3 M) and 7
Aug (83.2 ± 25.3 M) flights due to the overall rather low RH, this can potentially lead to high
deviations in the actual gas uptake coefficients, aqueous phase rate coefficients and to a lesser

Deleted: role in

Deleted: oxidation

Deleted: oxidant

Deleted: more than

Formatted: Subscript

Formatted: Subscript

Formatted: Subscript

Formatted: Font: Italic

Formatted: Subscript

Formatted: Subscript

Deleted: a

Deleted: micelle

Deleted: aircraft RH sensor

Deleted: addition

Deleted:

Deleted:

extent, pH (calculation of which does account for ionic strength, but is fairly under constrained under these conditions).

410 3 Results and discussion

3.1 Emission factors

415 The elemental sulfur EFs calculated for FIREX-AQ are comparable to previous reports. As described in section 2.3, flaming and smoldering delineation was determined by an MCE value of 0.9. For consistency with other FIREX-AQ reports, the fuel types listed remain as subcategories, but are combined for comparison to the comprehensive biomass burning fuel types listed by Andreae (2019). The FIREX-AQ agriculture category comprises measurements of residual burns of rice, corn, and soybean fields. Across the fuel types measured during FIREX-AQ (Fig. 2), we find that SO₂ is consistently larger than sulfate when calculated as EFs of elemental sulfur, indicating that, at most, a minor fraction of SO₂ (20–25%) is converted to sulfate within 1 hr downwind (or emitted directly as primary sulfate). Where data are not reported, this is due to either missing data or a low correlation with total carbon (R² < 0.5). The total sulfur EFs agree reasonably well with those reported by Andreae et al. (1988), measured in 420 the Amazon basin, in the range of 0.24–0.66 g S kg⁻¹ C.

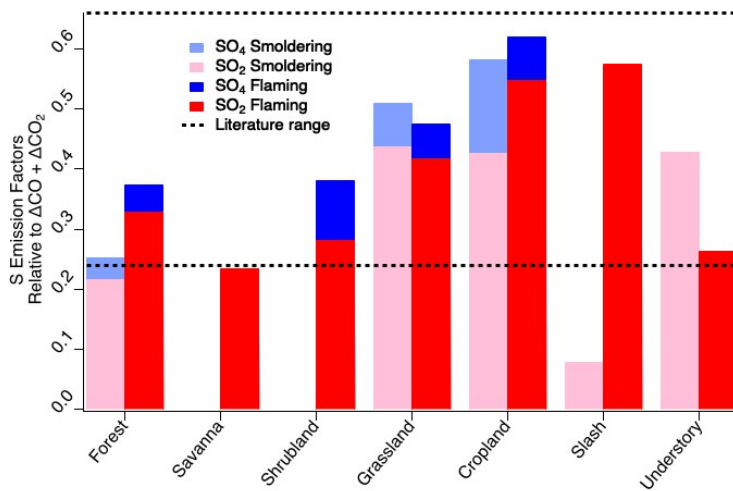


Figure 2. Elemental sulfur emission factors of SO₂ and sulfate by fuel type and combustion stage within 1 hr downwind compared to literature values of total sulfur emission factors.

430 No trend with MCE is observed for SO₂ EFs when separated by the various fuel types for smoldering and flaming conditions above MCE 0.85 for SO₂ and sulfate (Fig. 3). It has previously been suggested that EFs can be calculated based on MCE for use by the global climate modeling community. There have been conflicting opinions around this suggestion with some species showing relevant correlations while other species do not (Yokelson et al., 1996;

Deleted: 4

Deleted: in

Deleted: -

Deleted: is

Deleted: -

Deleted: when considering fuel types with measurements of

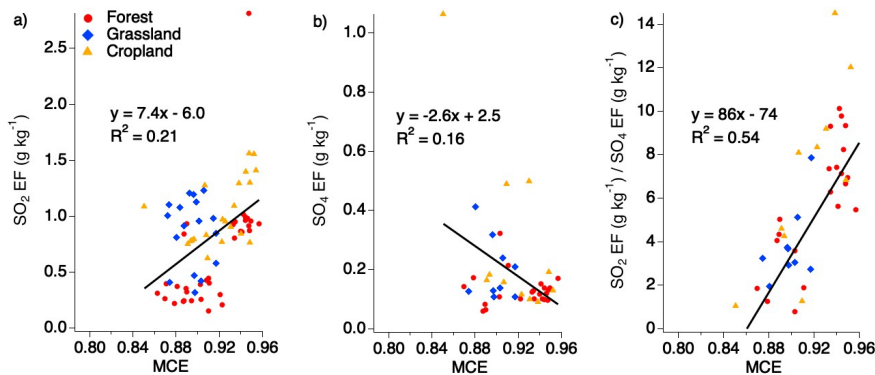
Deleted: as well as SO₂ and sulfate measurements

Deleted: (Fig.as well as

Deleted: measurements above MCE 0.85

445 Burling et al., 2011; Akagi et al., 2013). Considering all the EFs for SO₂, sulfate, and the ratio of
 SO₂ to sulfate under one hour shows that, individually, SO₂ and sulfate do not show strong
 correlations with MCE (Fig. 3). However, the ratio of the two produces a stronger correlation
 suggesting there may be a relationship in which more sulfate may be produced during
 smoldering combustion and more SO₂ emitted during flaming combustion. One possibility is that
 450 the smoke plumes from smoldering fires are more conducive to rapid conversion of SO₂ to
 sulfate such that the ratio of SO₂ and sulfate has significantly decreased by the time it is sampled.
 This could be due to a number of factors, including higher aerosol EF which, depending on the
 aerosol composition, could allow for more rapid aqueous phase oxidation. It is also possible that
 more primary sulfate is emitted from those plumes.

Averaging the flaming and smoldering EFs produces an overall SO₂ EF of 0.73 ± 0.43 g
 455 SO₂ kg⁻¹ C. This is within the combined variability of the Andreae (2019) compilation of flaming
 and smoldering EFs of 0.62 ± 0.75 g kg⁻¹ C, which excludes peat and laboratory fires. Separating
 the SO₂ EFs by combustion stage results in a flaming stage value of 0.80 ± 0.46 g kg⁻¹ C ($0.62 \pm$
 0.61 g kg⁻¹ C from Andreae, 2019) and a smoldering stage value of 0.62 ± 0.36 g kg⁻¹ C ($0.61 \pm$
 0.27 g kg⁻¹ C from Andreae, 2019). While the FIREX-AQ flaming stage value is considerably
 460 higher than the Andreae (2019) compilation, the two are within the combined variability of the
 observations. However, this higher average EF for the flaming stage FIREX-AQ measurements
 is strongly influenced by the large number of measurements of longleaf pine and agricultural
 fuels which had high EF values.



465 *Figure 3. Scatter plots of EFs for SO₂ (a), sulfate (b), and the ratio of SO₂ to sulfate (c) (within 1 hr downwind of each fire source) vs. MCE based on combined fuel types.*

470 Looking more closely at the different fuel types in comparison to the categories compiled
 by Andreae (2019), we see good agreement within the combined variability (Table 1 and Fig. 4).
 While the fuel types are categorized differently in this study, many still fit the characteristics of
 the categories listed in the compilation report allowing for comparison. Of the FIREX-AQ
 categories that allow for comparison with Andreae (2019), all EF data available are for the
 flaming stage.

475 The generally strong agreement between FIREX-AQ EFs and those in published
 inventories lends confidence to the quality of EFs underlying model emissions. Agricultural

burns exhibit the highest EFs. This was reported by Andreae (2019) as $0.80 \pm 0.71 \text{ g kg}^{-1} \text{ C}$ in the flaming stage, similar to $1.1 \pm 0.30 \text{ g kg}^{-1} \text{ C}$ reported here. The temperate forest category, comprised here of forest and slash, produces a combined EF of $0.70 \pm 0.51 \text{ g kg}^{-1} \text{ C}$ which is in excellent agreement with the Andreae (2019) value of $0.7 \pm 0.48 \text{ g kg}^{-1} \text{ C}$. Combining savanna, shrubland, grassland, and understory into the savanna/grassland category produces the largest difference in which the FIREX-AQ value of these combined fuels is $0.70 \pm 0.26 \text{ g kg}^{-1} \text{ C}$, whereas, Andreae (2019) reported a value of $0.47 \pm 0.44 \text{ g kg}^{-1} \text{ C}$; however, these values fit within the standard deviation.

Deleted: ,

Table 1. Comparison of the flaming stage SO_2 EFs ($\text{g kg}^{-1} \text{ C}$) by fuel type as measured during FIREX-AQ (left) to the compiled values reported in Andreae (2019) (right).

| Fuel Type (FIREX-AQ) | EF | StDev | Num tran ⁺ | Combined Categories | EF | StDev | Num stud [*] | Fuel Type (Andreae, 2019) |
|----------------------|------|-------|-----------------------|---------------------|------|-------|-----------------------|---------------------------|
| Forest | 0.66 | 0.49 | 35 | 0.70 ± 0.51 | 0.7 | 0.48 | 5 | Temperate forest |
| Slash | 1.15 | 0.38 | 3 | | | | | |
| Savanna | 0.47 | 0.06 | 2 | 0.70 ± 0.26 | 0.47 | 0.44 | 12 | Savanna/grassland |
| Shrubland | 0.56 | | 1 | | | | | |
| Grassland | 0.83 | 0.29 | 6 | | | | | |
| Understory | 0.53 | | 1 | | | | | |
| Cropland | 1.09 | 0.30 | 16 | - | 0.8 | 0.71 | 10 | Agriculture |

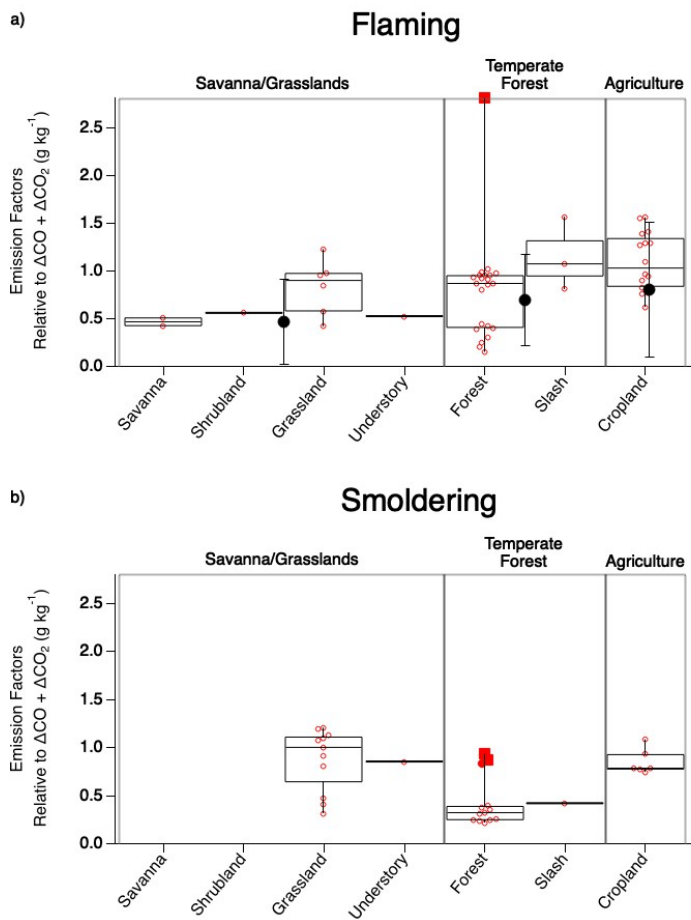
⁺Num tran indicates the number of transects measured within 1 hr downwind of the fire source measured during FIREX-AQ.

^{*}Num stud indicates the number of studies included in the Andreae (2019) compilation.

Deleted: Andreae

The categories measured during FIREX-AQ that do not overlap with the Andreae (2019) compilation reflect smoldering conditions. For the most part, the majority of the smoldering stage SO_2 EFs exhibit lower values than the flaming stage by approximately 21–63% (Fig. 4). The two FIREX-AQ categories (grassland and understory) which show smoldering SO_2 EFs to be larger than the flaming stage suggest the need for additional measurements to build statistical confidence.

Deleted: -



505 *Figure 4. Comparison of SO₂ EF values observed during flaming (a) and smoldering (b)*
combustion across fuel types sampled during FIREX-AQ. The box upper edge represents the
75th percentile and the lower edge the 25th percentile with the median shown by the middle line.
The whiskers represent the minimum and maximum observed values with the open circles
representing each observation and the solid red circle representing a potential outlier. The large
510 *solid black circles with error bars depicting 1 standard deviation in panel (a) show*
corresponding average Andreae (2019) values.

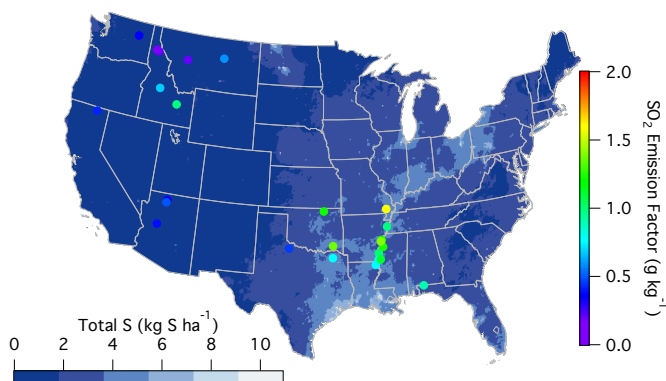
515 **3.2 Emission factor variability**

The variability observed amongst the different fuel types may partly reflect variability in surface S content stemming from wet and dry deposition. Although this source of sulfur has significantly decreased in the U.S. over the last two decades, the highest emission factors during FIREX-AQ were observed within the regions of the U.S. that typically experience the largest sulfur deposition rates as reported by the National Atmospheric Deposition Program (2022) (Fig. 5).

520 Sulfur-containing fertilizers may also enhance S content in smoke. Sulfur aids plant uptake of nitrogen, and decreasing sulfur deposition over the last two decades has led to an increased use of sulfur additives in fertilizers (Hinckley et al., 2020). Hinckley et al. (2020) report this sulfur application to range from around 20–300 kg S ha⁻¹ yr⁻¹, which occurs in the form of inorganic sulfate or elemental sulfur (Solberg et al., 2011). Given that the average yield of corn within the U.S. is 168 bushels per acre, a sulfur application of 20 kg S ha⁻¹ yr⁻¹ would result in 12 g S kg⁻¹ C in its composition. Assuming 10% of this added sulfur remains after harvest and runoff and is present in the residual material that is burned, the remaining 1.2 g S kg⁻¹ could in part explain the enhanced emission factors in those regions (U.S. Department of Agriculture, 2020). Therefore, the observed variability in emission factors throughout the U.S. may be in part explained by the sulfur availability to the plants and soils, either from deposition or fertilizer use, resulting in larger emission factors from certain locations when burned.

Deleted: -

Deleted: -



535 *Figure 5. National Atmospheric Deposition Program (2022) reported sulfur deposition rates (<https://nadp.slh.wisc.edu/committees/tdep/#tdep-maps>) compared to SO₂ EFs (closed circles) by geographical location as measured during FIREX-AQ for all fuel types.*

540 **4 Chemical Evolution of Sulfur**

After emission, SO₂ oxidizes to sulfate via both gas- and condensed-phase processes. Discrepancies reported by previous studies of modeled sulfate compared to measurements suggest that the conversion chemistry of SO₂ to sulfate is not fully understood. In this section, we combine FIREX-AQ observations with a detailed chemical box model to evaluate the chemical mechanisms of SO₂ to sulfate conversion.

4.1 Temperature dependence of sulfate production efficiency

550

The balance of gas and particle phase sulfur between SO₂ and sulfate exhibits a marked temperature dependence amongst the cumulative flights while remaining generally constant during individual flights (Fig. 6). The fewer observations at temperatures below 265 K is the result of the range of aircraft altitude sampled during this study. However, the decreasing trend shown by the numerous measurements between 265–283 K support the suggestion of lower SO₂ concentrations compared to sulfate at the lower temperatures. Sulfate is >90% of the sum at temperatures below 265K, while above 285 K SO₂ and sulfate are equally balanced which is likely due to the quasi-second order process of heterogeneous oxidation in a plume (Freiberg, 1978). The noisy, but overall positive trend between 265–283 K suggests rapid chemistry after emission. Conversion of SO₂ to sulfate generally increases with decreasing temperature due to increased aerosol water content and SO₂ and oxidant solubility, but the rapid change observed in this temperature regime also requires aqueous phase sulfur oxidation (Pattantyus et al., 2018).

555

560

The majority of sulfur oxidation occurs in the aqueous phase. As observed during the 3 August flight, calculation of the contribution of OH to the decrease in SO₂ by applying an OH concentration of $2 \times 10^6 \text{ cm}^{-3}$ (Liao et al., 2021) produces a negligible SO₂ decay compared to the dilution normalized mixing ratio of SO₂ (Fig. S2). Similar behavior is expected for other flights due to similar conditions of limited photolysis near the center of the smoke plume.

565

Recent studies have suggested HCHO to be an important aqueous phase oxidant at reduced temperatures (Moch et al., 2018; Song et al., 2021). However, HCHO is also an indicator of smoke age with mixing ratios typically being largest nearest to the fire source (Liao et al., 2021). Considering measurements acquired when the HCHO mixing ratio is high (> 25 ppb), implicitly filtering out aged smoke, the slope of the SO₂ to total sulfate ratio over the 265–283 K temperature regime (0.04) shows a stronger correlation with temperature ($R^2=0.74$) (Fig. 6b, black line). Further limiting the effect of chemical aging by analyzing only those measurements within 1 hr of the fire source, the conversion of SO₂ to sulfate is observed to be approximately 65% slower (Fig. 6b, red line) in the 265–283 K temperature range. This is consistent with heterogeneous chemistry in that aging occurs more rapidly at higher temperatures. While sulfate measurements within 1 hr of the fire source could be due to primary emission, this is expected to be a small fraction compared to SO₂ as shown in Fig. 2 and primary emission would not exhibit the temperature dependence observed here.

570

575

Other sulfate species contribute to sulfur conversion during this temperature regime. There were several periods identified during these flights in which organosulfur species were recognized to be a significant fraction of the AMS sulfate measurement. These measurements only occurred within the temperature range 270–285 K. When organosulfur was present in plume transects within 1 hr downwind of the fire source, the SO₂ to total S ratio decreased with decreasing temperature 23% faster than in transects of fresh plumes when organosulfur was not present.

580

585

These findings emphasize the importance of temperature in combination with smoke age and organosulfur production on the conversion of SO₂ to sulfate and is further investigated in section 4.2.1.

590

Deleted: in which the lowest temperatures are correlated with the highest altitude of 6 km

Deleted: -

Deleted: -

Deleted: -

Deleted: -

Deleted: are

Deleted: ing

Deleted: -

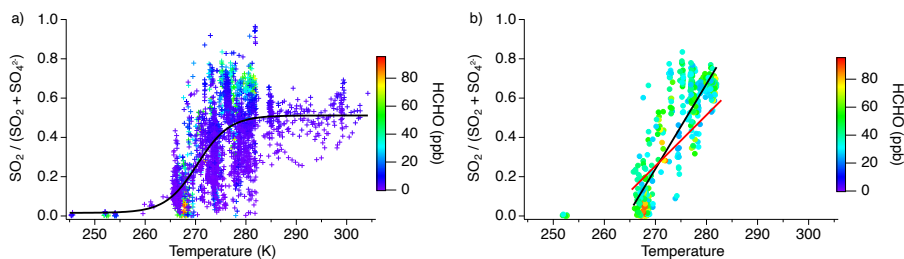


Figure 6. Fractional sulfur conversion as a function of temperature a) including all smoke ages with a sigmoid fit and b) only measurements with HCHO > 25 ppb with the black line indicating the linear fit through the data at all ages between 265–283 K and the red line indicating the linear fit through the measurements within 1 hr of emission in the same temperature regime.

Deleted: -

4.2 Model results

4.2.1 Williams Flats 3 August 2019 flight

Select time series relating to the conversion of SO₂ to sulfate for the 3 August 2019 flight are shown in Fig. S3. Altitude and temperature were constant, around 3 km and 280 K, for both passes of about 10 transects each. Actinic fluxes trended downward for the second pass as dusk approached. Thermodynamic modeling suggests an average pH value of 5.3 (range of -2 to 8) over the length of the plume transects, but a possible increase in LWC by a factor of 2–3 during the second pass with an average of $2 \times 10^{-6} \text{ g sm}^{-3}$. Because the conditions of this flight are relatively consistent between passes, the measurements of both passes are combined for comparison to the model with pH and LWC held constant. Modeling results of this flight with the inclusion of all known gas- and aqueous-phase S(IV) pathways (Table S1) are shown in Fig. 7 with a conservatively assumed 30% uncertainty shown. This uncertainty range encompasses the uncertainties associated with the mechanism of aqueous phase uptake and chemical rate constants occurring at the specified LWC and pH.

Deleted: -

Deleted: ($2 \times 10^{-4} \text{ g sm}^{-3}$)

Deleted: oxidation

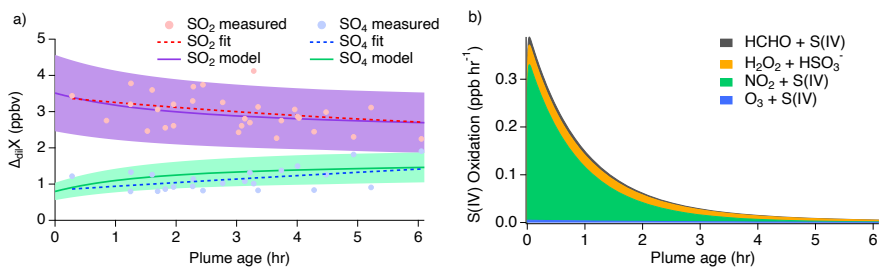


Figure 7. (a) Dilution corrected ($\Delta_{dil}X$) measurements of 3 August 2019 shown by the markers and measurement fits shown by the dashed lines compared to the SO₂ and sulfate model results represented by the solid lines with shading denoting an estimated 30% model uncertainty. The

Deleted: M

635 sulfate (SO_4) measurements represent total sulfate which potentially includes organosulfur. (b)
Stacked modeled S(IV) oxidation rates leading to sulfate and HMS production.

640 The model reproduces the general measurement trend of the 3 August flight for both SO_2
and sulfate (Fig. 7a). Model results for NO, NO_2 , NO/ NO_2 , O_3 , HCHO, and H_2O_2 are compared
to the measurements for each model in Fig. S4 showing good agreement for the 3 August flight.
645 In accordance with the sulfate measurements, the modeled sulfate represents the sum of sulfate
and HMS (the latter representing OS). A small, yet important, change is observed for the SO_2
and sulfate measurements with SO_2 decreasing by a linear slope of 0.15 ppb hr^{-1} and sulfate
increasing by a linear slope of 0.26 ppb hr^{-1} . The decrease in the S(IV) reactions (Fig. 7b) further
demonstrates this. The largest increase in these reactions is observed within the first 15 min, but
650 the decrease in these reactions over the remaining 6 hrs indicates a slowing of this conversion.
Under the conditions of this flight, the model indicates that aqueous phase oxidation by NO_2 and
 H_2O_2 are the dominant pathways leading to inorganic sulfate formation with little S(IV) reaction
by HCHO and O_3 (Fig. 7b). This is in contrast to what has been previously expected of aerosol
S(IV) oxidation which has been thought to be dominated by ozone oxidation. However, the
650 higher NO_2 oxidation rate constant with increased pH reported by Liu and Abbatt (2021) for
non-ideal solutions increases the significance of this reaction.

Deleted: oxidation

4.2.2 Williams Flats 7 August 2019 flight

655 The 7 August 2019 flight shows distinct differences between the two passes (Fig. S5); therefore,
the flight has been differentiated into the first pass (first full set of transects) and second pass
(second full set of transects). It is also during this flight that the largest OS contribution has been
reported for the AMS measurements during the FIREX-AQ wildfire flights.

660 The first pass was measured around 4 km and 276 K with an estimated dilution factor of
approximately $8 \times 10^{-5} \text{ s}^{-1}$ and limited cloud presence. A pH of around 7.2 was estimated for
this flight with an aerosol LWC of approximately $1 \times 10^{-7} \text{ g sm}^{-3}$. Both NO_2 and CO decrease
at similar rates while HCHO remains relatively stable around 40 ppb and O_3 shows a decrease
compared to the air outside of the plume for the first six transects (Fig. S6). SO_2 and sulfate are
fairly similar with a few instances of sulfate surpassing SO_2 in addition to a moderate fraction of
665 OS observed during this pass.

670 The increased altitude of the second pass is associated with an 8 K decrease in
temperature relative to the first pass. The dilution factor for this pass was determined to be
slower at around $3 \times 10^{-5} \text{ s}^{-1}$. The difference in these dilution factors could be due to measuring
at different altitudes or the result of a sampling artifact due to measuring in different sections of
the plume, however, there is not enough information available to determine the exact cause. NO_2
appears to decrease more slowly in comparison to CO which remains relatively constant after the
plume has moved away from the clouds. In addition, ozone, which shows the same trend as O_x ,
appears to be consumed more quickly in transects in which clouds were observed, suggesting
rapid uptake within the clouds, in addition to the fast reaction with NO producing the additional
675 NO_2 . This additional NO_2 in combination with limited photochemistry as a result of decreasing
actinic flux (Fig. S7) due to approaching dusk conditions slows the decreasing NO_2 trend
observed during this pass. Furthermore, ISORROPIA calculations indicate a 10-fold increase in
aerosol LWC in the presence of clouds compared to the first pass. This is likely due to the
decrease in temperature (268 K) and larger relative humidity. The presence of clouds decreases

Deleted: rise in

Deleted: for

685 downwind concurrently with a decrease in relative humidity, but aerosol LWC remains high. Lastly, this pass shows SO₂ is nearly depleted in the center of the plume (Fig. S5) while sulfate increases substantially with a rather significant fraction of OS being observed (Fig. S8).

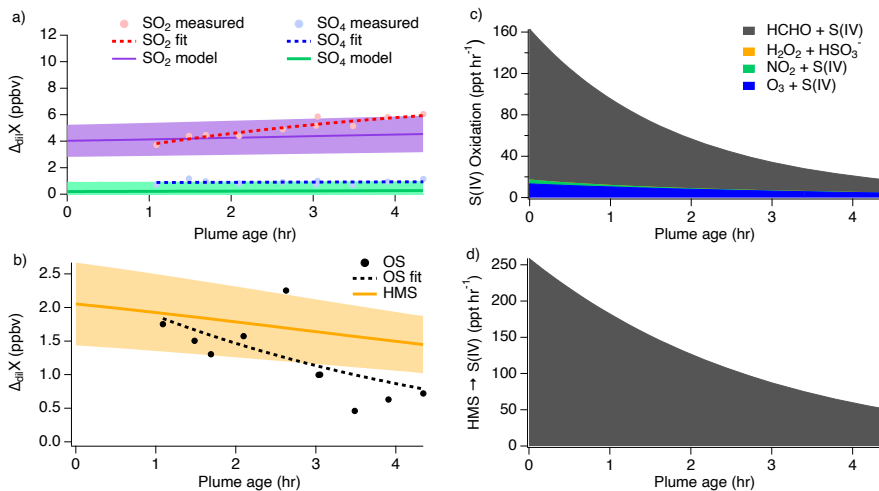
690 Due to these distinct differences between passes, each pass was modeled separately with the OS contribution reported independently from the sulfate measurements and model results. The modeled oxidation compounds (Fig. S4) show generally good agreement with the measurements for these passes; however, some discrepancies are observed due to measuring different parts of the plume. Results of the first pass are shown in Fig. 8 and the second pass shown in Fig. 9; both show good agreement between the model and measurements with ozone and NO₂ as the largest contributors to sulfate production during this flight. However, the majority of modeled S(IV) reaction occurs through the HCHO pathway rapidly producing HMS.

695 The first pass shows SO₂ increasing downwind, which is unexpected because SO₂ is considered to be a primary emission which typically decreases downwind as it is removed through oxidation. In addition, the measurements show a large OS mixing ratio following the first hour after emission before gradually decreasing downwind. This suggests that OS is either directly emitted from the fire source or very rapidly produced.

700 Clouds and large LWC were present throughout the majority of the second pass measurements (Figs. S5 and S6), significantly shifting the chemistry from that of the first pass. Figure 9 shows that modeled SO₂ is quickly taken up into the aqueous phase under higher LWC conditions ($6 \times 10^{-5} \text{ g sm}^{-3}$) and pH (7.2) with approximately 1.5 ppb going directly into sulfate production and the remaining 3 ppb of the initial SO₂ concentration being converted into HMS. These reaction processes occur promptly after emission, but they rapidly slow once all of the available initial SO₂ is depleted within the first 1-2 minutes. The exponential trends of the sulfate and OS measurements agree with the model results to within approximately 40%.

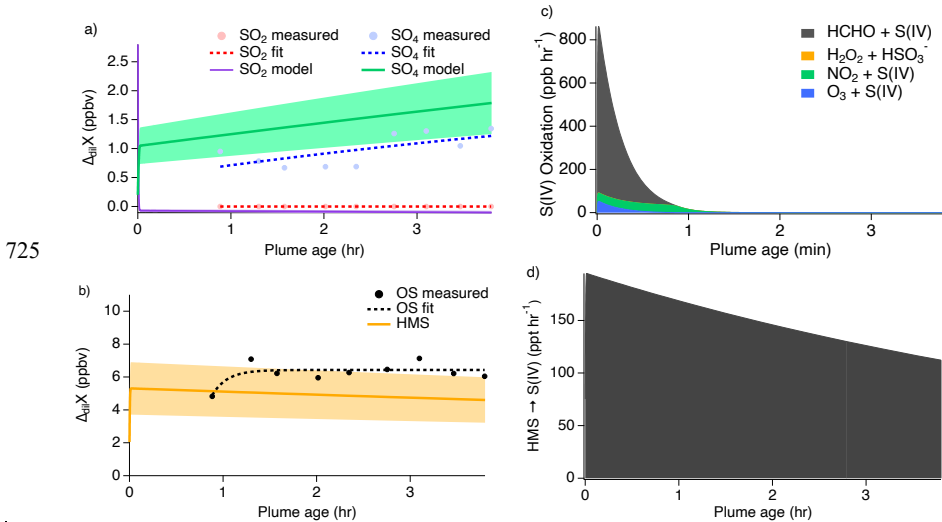
Deleted: ,
Deleted: ing
Deleted: oxidation

Deleted: these higher LWC conditions
Deleted: 1
Deleted: 3
Deleted: oxidation
Deleted: -



710 Figure 8. First pass dilution corrected ($\Delta_{dil}X$) measurements shown by the markers and measurement fits shown by the dashed lines compared to the model results represented by the

solid lines with shading denoting an estimated 30% model uncertainty for SO₂ and sulfate (a) and OS (b). Stacked modeled S(IV) oxidation rates (c) leading to sulfate and HMS production. HMS reverse reaction rate (d) reproducing S(IV).



725

730

Figure 9. Second pass dilution corrected ($\Delta_{dil}X$) measurements shown by the markers and measurement fits shown by the dashed lines compared to the model results represented by the solid lines with shading denoting an estimated 30% model uncertainty for SO₂ and sulfate (a) and OS (b). Stacked modeled S(IV) oxidation rates (c) leading to sulfate and HMS production. HMS reverse reaction rate (d) reproducing S(IV).

735

740

745

Comparing the 3 August and 7 August flights, the main differences leading to the different S(IV) reaction pathways are the pH and HCHO mixing ratios. Average pH on the 3 August flight was 5.3; whereas the 7 August flight experienced neutral conditions with a pH around 7.2. The initial HCHO mixing ratio was estimated to be 30 ppb for the 3 August flight and 50 ppb for the 7 August flight. While liquid water content plays a significant role in affecting the HMS reversal rate, each of these flights remained within the wet aerosol characterization with a calculated LWC of $2 \times 10^{-6} \text{ g sm}^{-3}$ for the 3 August flight and $6 \times 10^{-6} \text{ g sm}^{-3}$ (4 km) and $6 \times 10^{-5} \text{ g sm}^{-3}$ (5 km) for the 7 August flight.

The importance of HMS as a S(IV) reservoir and its conversion into sulfate or into gas-phase SO₂ largely depends on the varying conditions of LWC. Under neutralized conditions (7.2), the model reproduces the observed trends of all three compounds under these wet aerosol conditions. As discussed further in section 4.2.3, the higher pH of this flight increases the rate of HMS reversal back into S(IV) by a factor of six. Because of the low LWC of the first pass, heterogeneous uptake is limited and causes the rates of S(IV) reaction to significantly decrease. S(IV) evaporation then enhances gas phase SO₂ in transported smoke, consistent with similar rates of HMS decay and SO₂ growth. As a result, very little sulfate is produced during this pass at a rate of approximately 4 ppt hr⁻¹ primarily due to S(IV) oxidation by ozone. However, the

- Deleted: 4
- Deleted: which also occurs between the LWC for
- Deleted: the 7 August flight of
- Deleted: 1
- Deleted: 7
- Deleted: 1
- Deleted: 3
- Deleted: →
- Formatted: Indent: First line: 0.5"
- Deleted: oxidation

760 higher LWC conditions of the second pass allow S to remain in the aqueous phase. The small increase in sulfate of approximately 500 ppt over the course of the flight can be explained by a small fraction of HMS, on the order of 120–190 ppt hr⁻¹, which undergoes a reverse reaction decomposing back into S(IV) before being oxidized to produce sulfate (Fig. 9d).

765 The SAGA MC/IC instrument detects HMS as S(IV), which cannot be separated from HSO₃⁻ and SO₃²⁻ and is therefore subject to interference from high concentrations of gas-phase SO₂. As shown in Fig. S9, MC sulfate measurements show similar concentrations to the AMS inorganic sulfate measurements during both passes. The AMS total sulfate is slightly larger than the MC sulfate in the first pass, but considerably larger during the second pass. The MC S(IV) (reported as SO₃) was similar to AMS SO₄(org) on the first pass, but did not increase with AMS SO₄(org) during the second pass suggesting that HMS may have been the majority of the organosulfur concentrations measured during the first pass but that an additional unknown organosulfur was much more abundant than HMS during the second pass. Therefore, it appears that the modeled HMS exceeds measurements on the second pass.

770 There are two potential explanations for the good agreement between the observed organosulfur concentration from the second pass and the modeled HMS. It is possible that during the very rapid uptake of SO₂ into the aqueous phase, (1) additional organosulfur species may be produced or (2) the additional organosulfur species are the result of further reactions of HMS suggesting that the model is correctly reproducing the HMS formation chemistry, but indicating that the model aqueous phase chemistry is incomplete. Both of these potential explanations require that the measured organosulfur species behave similarly to HMS in their rates of formation and termination in order to explain the good agreement between the modeled HMS and measured organosulfur concentrations. In addition, these explanations would require that the organosulfur species are not identified as S(IV) in ion chromatography measurements. It is a potential possibility with the large mixing ratios of HCHO and H₂O₂ observed in these fire plumes that the chemistry of hydroxymethyl hydroperoxide as a result of HCHO and H₂O₂ reaction could be influencing the organosulfur production and should be considered in future studies (Dovrou et al., 2022). While the modeling allows for significant insight into the identity and formation mechanisms of aerosol sulfur, there is not enough evidence available from these measurements to conclusively explain all of the AMS and SAGA MC/IC sulfur observations.

790 4.2.3 Model HMS sensitivity analysis

795 We performed a model sensitivity analysis to investigate the relevance of organosulfur behavior under the conditions of the HMS rates of production and termination in different environments by varying the model LWC (10⁻⁶–1 g sm⁻³), pH (1–8), temperature (260–280 K), and HCHO (10–90 ppb) individually while holding the other parameters constant at the 3 August flight conditions (T = 280 K, pH = 5.3, and LWC = 2 × 10⁻⁴ g sm⁻³) due to the more simplified chemistry occurring during this flight.

800 Variations in LWC (Fig. 10a) show that aerosols with less LWC produce minimal amounts of sulfate and HMS, but that HMS makes up between 5 and 45% of the combined concentrations. The HMS fraction shows the largest contribution as LWC increases into the cloud regime at which point sulfate production begins to decrease with a rapid increase in HMS. While the typical LWC range estimated for these fires is 10⁻⁷–10⁻² g sm⁻³, this indicates that the chemistry of the smoke will change substantially with cloud interactions. LWC is shown to

Deleted: -

Deleted: +

Deleted: S8

Deleted: 8

Deleted: organosulfur portion of the total

Deleted: the first pass, but a considerably smaller value in comparison during the second pass. This suggests

Formatted: Subscript

Deleted: This

Deleted: s

Deleted: ,

Deleted: -

Deleted: -

Deleted: -

Deleted: -

be an important variable in the ratio of the formation of HMS to sulfate; however, this ratio trend is indicative of conditions at pH 5.3 and will vary under differing pH conditions.

820 The pH dependence of the ratio of HMS / (SO₄ + HMS) is shown in Fig. 10b in which HMS formation is more active as the acidity decreases. At acidic pH values, representative of typical tropospheric aerosol (Nault et al., 2021), a negligible amount of HMS contributes to the combined concentrations. Above pH 4, HMS contribution begins to increase followed by a more rapid increase after pH 6. The maximum HMS contribution is reached around pH 7.3 before
825 rapidly decreasing at higher values.

The ratio of HMS production and reverse reactions varies with pH with the reverse reaction becoming more substantial at higher pH (Fig. 11). Under aerosol LWC conditions, the rate of the HMS reverse reaction is up to 3 times larger than the rate of HMS production. As LWC increases into the cloud regime, the rate of the HMS reverse reaction increases further to approximately two orders of magnitude larger than HMS production around pH 7. However, a
830 reduction in temperature shifts this dependence to higher pH decreasing the rate of HMS reversal at the same pH.

While temperature and HCHO concentration are key factors controlling HMS production, these factors alone under low LWC and pH result in minimal HMS (Fig. S10). HMS production
835 increases with decreasing temperature; however, under the conditions of the 3 August flight, HMS only reaches a maximum value of 5 ppt at 260 K which is approximately 5% of the modeled sulfate. Similarly, a minimal amount of HMS is produced with varied HCHO, but the ratio of HMS to the sum of HMS and sulfate increases linearly with HCHO at a rate of 1.5 ppt ppb⁻¹ HCHO.

840 The conditions that most largely affect HMS are LWC and pH. Due to the significance of LWC to HMS production and reversal, it is likely that aqueous aerosols, fog, cloud droplets, and possibly ice crystals will be most impactful on HMS production. Because the rainwater pH of areas such as the Western U.S. and Eastern China can reach much less acidic pH levels due to increased ammonia emissions, it is likely that these areas will be more susceptible to HMS
845 production (Keresztesi et al., 2020; Qu and Han, 2021). Together, these conditions indicate that highly polluted areas which experience higher pH and greater LWC will likely be influenced by this chemistry. Therefore, the production of HMS should be an important consideration for air quality in areas such as agricultural regions which experience enhanced emissions of ammonia, likely increasing the pH, as well as geographical locations which may promote fog formation.

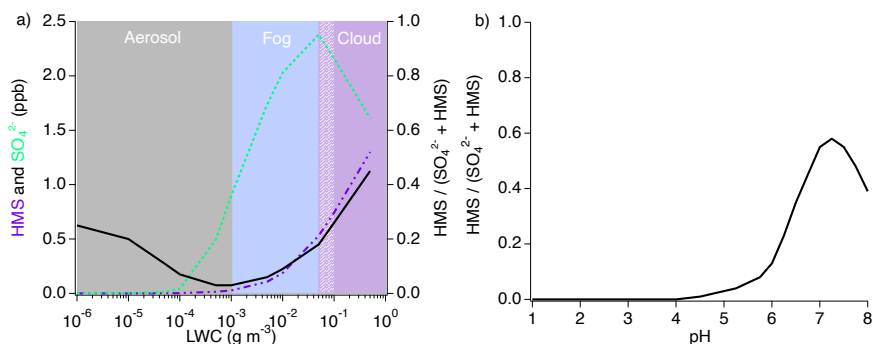
850 This would include areas such as Beijing, the Uinta Basin, and Bakersfield, CA, which have observed severe haze formation and have the potential to be affected by HMS.

Deleted: S9

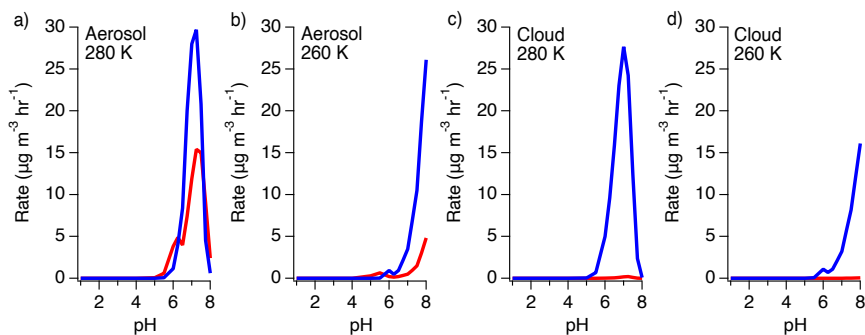
Deleted: 9

Deleted: h

Deleted: basin



860 Figure 10. Sensitivity analysis of HMS formation under individually varied LWC and pH conditions. The black line in each figure represents the ratio of the modeled HMS mixing ratio to the sum of the modeled inorganic sulfate and HMS. The shading in b) reflects the typical rainwater pH for each region.



865 Figure 11. Rates of HMS production (red) and reversal (blue) under aerosol and cloud conditions at 280 K and 260 K.

5. Conclusions

870 SO₂ plays an important role in sulfate aerosol formation and thus air quality and climate forcing. Therefore, understanding the sources and evolution of SO₂ emissions in a changing climate are essential. The emission factors determined from the FIREX-AQ mission under flaming conditions show good agreement with the compilation reported by Andreae (2019). This provides confidence for the same categories under smoldering conditions for which there are no reported measurements from previous studies. No distinct correlation is observed for SO₂ emission factors based on MCE; however, it remains unclear if fire MCE influences the ratio of SO₂ and sulfate emission factors. With biomass burning events increasing worldwide, this study suggests that the resulting SO₂ emission factors will be more dependent on geographical location and land use, and less dependent on combustion phase and fuel type. Areas that incur more sulfur

880 deposition from coal burning or application through fertilizer use, will likely produce larger SO₂ emission factors.

| Modeling with inclusion of the HCHO reaction chemistry, producing HMS, shows good agreement with the measurements. However, the differentiation of HMS from sulfate through the SAGA MC/IC measurements indicates that HMS can be over-predicted. While HMS is
885 potentially directly emitted from the fire source, a large organosulfur concentration is observed that has not yet been identified. Because the modeled HMS is similar to the measured organosulfur fraction, it is expected that the additional organosulfur species likely exhibit similar rates of production and termination as HMS. The importance of the HMS, or similar species, reverse reaction is also made apparent by the ability to act as an S(IV) reservoir. This allows
890 these species to produce sulfate or SO₂ further downwind depending on the LWC and pH.

Environments that experience high LWC and pH are expected to be the most influenced by this chemistry. This includes regions that experience higher ammonia emissions and are geographically or meteorologically subject to greater cloud or fog formation. As a result, this chemistry should be considered when assessing severe haze events as a result of either biomass
895 burning or industrial pollution.

Plain Language Summary

| Biomass burning sulfur dioxide (SO₂) emission factors range from 0.27–1.1 g kg⁻¹ C. Biomass
900 burning SO₂ can quickly form sulfate and organosulfur, but these pathways are dependent on liquid water content and pH. Hydroxymethanesulfonate (HMS) appears to be directly emitted from some fire sources, but is not the sole contributor to the organosulfur signal. It is shown that HMS and organosulfur chemistry may be an important S(IV) reservoir with the fate dependent on the surrounding conditions.

905

Keywords

Sulfur dioxide, hydroxymethanesulfonate, emission factors, biomass burning

910 *Data and code availability.* The data collected for FIREX-AQ are available from the NASA/NOAA FIREX-AQ data archive: <https://www-air.larc.nasa.gov/cgi-bin/ArcView/firexaq>. The Framework for 0-D Atmospheric Modeling code is available from the AirChem/F0AM archive: <https://github.com/AirChem/F0AM> (doi.org/10.5281/zenodo.5752566).

915 *Author contribution.* The research was designed by PSR and AWR. Measurement contributions were provided by all authors. The modeling was performed by PSR and GMW. The paper was written by PSR with contributions from all coauthors.

920 *Competing interests.* The authors declare that they have no conflict of interest.

Acknowledgements. P.S.R. and A.W.R. acknowledge support from NASA's Upper Atmosphere Composition Observations program. MD, MS, and BW have received funding from the European Research Council (ERC) under the European Union's Horizon 2020 research and innovation framework programme under grant agreement No. 640458 (A-LIFE), and from
925 University of Vienna. HG, PCJ, and JLJ were supported by NASA 80NSSC18K0630 and

Deleted: oxidation

Formatted: Superscript

80NSSC21K1451 and NSF AGS-1822664. GMW, TFH, RAH, JMS, and JL acknowledge support from the NASA Tropospheric Composition program and the NOAA AC4 program (NA17OAR4310004). SRH and KU are funded under NASA grant 80NSSC18K0638. The National Center for Atmospheric Research is sponsored by the National Science Foundation. We would like to thank the NASA DC-8 crew and management team for support during FIREX-AQ integration and flights. Data from FIREX-AQ are available at (<https://www-air.larc.nasa.gov/cgi-bin/ArcView/firexaq>).

935 **References**

Adachi, K., Dibb, J. E., Scheuer, E., Katich, J. M., Schwarz, J. P., Perring, A. E., Mediavilla, B., Guo, H., Campuzano-Jost, P., Jimenez, J. L., Crawford, J., Soja, A. J., Oshima, N., Kajino, M., Kinase, T., Kleinman, L., Sedlacek III, A. J., Yokelson, R. J., Buseck, P. R.: Fine Ash-Bearing Particles as a Major Aerosol Component in Biomass Burning Smoke, *J. Geophys. Res. Atmos.*, 127(2), <https://doi.org/10.1029/2021JD035657>, 2022.

Akagi, S. K., Yokelson, R. J., Burling, I. R., Meinardi, S., Simpson, I., Blake, D. R., McMeeking, G. R., Sullivan, A., Lee, T., Kreidenweis, S., Urbanski, S., Reardon, J., Griffith, D. W. T., Johnson, T. J., and Weise, D. R.: Measurements of reactive trace gases and variable O₃ formation rates in some South Carolina biomass burning plumes, *Atmos. Chem. Phys.*, 13, 1141–1165, <https://doi.org/10.5194/acp-13-1141-2013>, 2013.

Albrecht, B. A.: Aerosols, cloud microphysics, and fractional cloudiness, *Science*, 245, 1227-1230, 1989.

Andreae, M. O., Browell, E. V., Garstang, M., Gregory, G. L., Harriss, R. C., Hill, G. F., Jacob, D. J., Pereira, M. C., Sachse, G. W., Setzer, A. W., Silva Dias, P. L., Talbot, R. W., Torres, A. L., Wofsy, S. C.: Biomass-Burning Emissions and Associated Haze Layers Over Amazonia, *J. Geophys. Res. Atmos.*, 93(D2), 1509-1527, <https://doi.org/10.1029/JD093iD02p01509>, 1988.

Andreae, M. O.: Emission of trace gases and aerosols from biomass burning – an updated assessment, *Atmos. Chem. Phys.*, 19, 8523–8546, <https://doi.org/10.5194/acp-19-8523-2019>, 2019.

Brock, C. A., Wagner, N. L., Anderson, B. E., Attwood, A. R., Beyersdorf, A., Campuzano-Jost, P., Carlton, A. G., Day, D. A., Diskin, G. S., Gordon, T. D., Jimenez, J. L., Lack, D. A., Liao, J., Markovic, M. Z., Middlebrook, A. M., Ng, N. L., Perring, A. E., Richardson, M. S., Schwarz, J. P., Washenfelder, R. A., Welti, A., Xu, L., Ziemba, L. D., and Murphy, D. M.: Aerosol optical properties in the southeastern United States in summer – Part 1: Hygroscopic growth, *Atmos. Chem. Phys.*, 16, 4987–5007, 2016.

Burling, I. R., Yokelson, R. J., Griffith, D. W. T., Johnson, T. J., Veres, P., Roberts, J. M., Warneke, C., Urbanski, S. P., Reardon, J., Weise, D. R., Hao, W. M., and de Gouw, J.: Laboratory measurements of trace gas emissions from biomass burning of fuel types from the southeastern and southwestern United States, *Atmos. Chem. Phys.*, 10, 11115–11130, <https://doi.org/10.5194/acp-10-11115-2010>, 2010.

- 975 Burling, I. R., Yokelson, R. J., Akagi, S. K., Urbanski, S. P., Wold, C. E., Griffith, D. W. T., Johnson, T. J., Reardon, J., and Weise, D. R.: Airborne and ground-based measurements of the trace gases and particles emitted by prescribed fires in the United States, *Atmos. Chem. Phys.*, 11, 12197–12216, <https://doi.org/10.5194/acp-11-12197-2011>, 2011.
- 980 Canagaratna, M. R., Jayne, J. T., Jimenez, J. L., Allan, J. D., Alfarra, M. R., Zhang, Q., Onasch, T. B., Drewnick, F., Coe, H., Middlebrook, A., Delia, A., Williams, L. R., Trimborn, A. M., Northway, M. J., Decarlo, P. F., Kolb, C. E., Davidovits, P., and Worsnop, D. R.: Chemical and microphysical characterization of ambient aerosols with the Aerodyne Aerosol Mass Spectrometer, *Mass Spectrom. Rev.*, 26, 185–222, 2007.
- 985 Chan, C.K., Yao, X.: Air pollution in mega cities in China. *Atmospheric Environment* 42, 1-42, 2008.
- 990 Cheng, Y., Zheng, G., Wei, C., Mu, Q., Zheng, B., Wang, Z., Gao, M., Zhang, Q., He, K., Carmichael, G., Pöschl, U., and Su, H.: Reactive nitrogen chemistry in aerosol water as a source of sulfate during haze events in China, *Sci. Adv.*, 2(12) 1-11, DOI: 10.1126/sciadv.1601530, 2016.
- 995 Cruz, C. N., Dassios, K. G., and Pandis, S. N.: The effect of dioctyl phthalate films on the ammonium nitrate aerosol evaporation rate, *Atmos. Environ.*, 34, 3897-3905, doi: 10.1016/S1352-2310(00)00173-4, 2000.
- 1000 D'Ambro, E. L., Moller, K. H., Lopez-Hilfiker, F. D., Schobesberger, S., Liu, J., Shilling, J. E., Lee, B. H., Kjaergaard, H. G., and Thornton, J. A.: Isomerization of Second-Generation Isoprene Peroxy Radicals: Epoxide Formation and Implications for Secondary Organic Aerosol Yields, *Environ. Sci. Technol.*, 51(9), 4978-4987, <https://doi.org/10.1021/acs.est.7b00460>, 2016.
- 1005 Dassios, K. G., and Pandis, S. N.: The mass accommodation coefficient of ammonium nitrate aerosol, *Atmos. Environ.*, 33, 2993-3003, doi: 10.1016/S1352-2310(99)00079-5, 1999.
- 1010 Day, D. A., Campuzano-Jost, P., Nault, B. A., Palm, B. B., Hu, W., Guo, H., Wooldridge, P. J., Cohen, R. C., Docherty, K. S., Huffman, J. A., de Sá, S. S., Martin, S. T., and Jimenez, J. L.: A Systematic Re-evaluation of Methods for Quantification of Bulk Particle-phase Organic Nitrates Using Real-time Aerosol Mass Spectrometry, *Atmos. Meas. Tech.*, <https://doi.org/10.5194/amt-15-459-2022>, 2022.
- 1015 DeCarlo, P. F., Kimmel, J. R., Trimborn, A., Northway, M. J., Jayne, J. T., Aiken, A. C., Gonin, M., Fuhrer, K., Horvath, T., Docherty, K. S., Worsnop, D. R., and Jimenez, J. L.: Field-deployable, high-resolution, time-of-flight aerosol mass spectrometer, *Anal. Chem.*, 78, 8281–8289, <https://doi.org/10.1021/ac061249n>, 2006.
- Dibb, J. E., Talbot, R. W., Seid, G., Jordan, C., Scheuer, E., Atlas, Elliot, Blake, N. J., and Blake, D. R.: Airborne sampling of aerosol particles: Comparison between surface sampling at

- 1020 Christmas Island and P-3 sampling during PEM-Tropics B, *J. Geophys. Res.-Atmos.*, 108, 8230–8230, doi:10.1029/2001JD000408, 2002.
- Dovrou, E., Bates, K. H., Moch, J. M., Mickley, L. J., Jacob, D. J., and Keutsch, F. N.: Catalytic role of formaldehyde in particulate matter formation, *Proc. Natl. Acad. Sci.*, 119(6), <https://doi.org/10.1073/pnas.2113265119>, 2022.
- 1025 Dovrou, E., Lim, C. Y., Canagaratna, M. R., Kroll, J. H., Worsnop, D. R., and Keutsch, F. N.: Measurement techniques for identifying and quantifying hydroxymethanesulfonate (HMS) in an aqueous matrix and particulate matter using aerosol mass spectrometry and ion chromatography, *Atmos. Meas. Tech.*, 12, 5303–5315, <https://doi.org/10.5194/amt-12-5303-2019>, 2019.
- 1030 Farmer, D. K., Matsunaga, A., Docherty, K. S., Surratt, J. D., Seinfeld, J. H., Ziemann, P. J., and Jimenez, J. L.: Response of an aerosol mass spectrometer to organonitrates and organosulfates and implications for atmospheric chemistry, *Proc. Natl. Acad. Sci. U. S. A.*, 107, 6670–6675, 2010.
- 1035 Feinberg, A., Sukhodolov, T., Luo, B. P., Rozanov, E., Winkel, L. H. E., Peter, T. and Stenke, A.: Improved tropospheric and stratospheric sulfur cycle in the aerosol–chemistry–climate model SOCOL-AERv2, *Geosc. Model Dev.*, 12, 3863–3887, <https://doi.org/10.5194/gmd-12-3863-2019>, 2019.
- 1040 Ferek, R.J., Reid, J.S., Hobbs, P.V., Blake, D.R., and Liousse, C.: Emission factors of hydrocarbons, halocarbons, trace gases and particles from biomass burning in Brazil. *J. Geophys. Res. Atmos.*, 103, 32107–32118, <https://doi.org/10.1029/98jd00692>, 1998.
- Fiedler, V., Arnold, F., Ludmann, S., Minikin, A., Hamburger, T., Pirjola, L., Dörnbrack, A., and Schlager, H.: African biomass burning plumes over the Atlantic: aircraft based measurements and implications for H₂SO₄ and HNO₃ mediated smoke particle activation, *Atmos. Chem. Phys.*, 11, 3211–3225, <https://doi.org/10.5194/acp-11-3211-2011>, 2011.
- 1050 Fountoukis, C. and Nenes, A.: ISORROPIA II: a computationally efficient thermodynamic equilibrium model for K–Ca–Mg–NH–Na–SO–NO–Cl–HO aerosols, *Atmos. Chem. Phys.*, 7, 4639–4659, 2007.
- Freiberg, J.: Conversion Limit And Characteristic Time of SO₂ Oxidation In Plumes, *Atmos. Environ.* 12, 339–347, 1978.
- 1055 Fridlind, A. M., and Jacobson, M. Z.: A study of gas-aerosol equilibrium and aerosol pH in the remote marine boundary layer during the First Aerosol Characterization Experiment (ACE 1), *J. Geophys. Res.*, 105, 17325–17340. doi: 10.1029/2000jd900209, 2000.
- 1060 Fromm, M., Bevilacqua, R., Servranckx, R., Rosen, J., Thayer, J., Herman, J., and Larko, D.: Pyro-cumulonimbus injection of smoke to the stratosphere: Observations and impact of a super blowup in northwestern Canada on 3–4 August 1998, *J. Geophys. Res.*, 110, D08205, doi:10.1029/2004JD005350, 2005.

- 1065 Fry, J. L., Draper, D. C., Zarzana, K. J., Campuzano-Jost, P., Day, D. A., Jimenez, J. L., Brown, S. S., Cohen, R. C., Kaser, L., Hansel, A., Cappellin, L., Karl, T., Hodzic Roux, A., Turnipseed, A., Cantrell, C., Lefer, B. L., and Grossberg, N.: Observations of gas- and aerosol-phase organic nitrates at BEACHON-RoMBAS 2011, *Atmos. Chem. Phys.*, 13, 8585–8605, 2013.
- 1070 Guo, H., Campuzano-Jost, P., Nault, B. A., Day, D. A., Schroder, J. C., Kim, D., Dibb, J. E., Dollner, M., Weinzierl, B., and Jimenez, J. L.: The importance of size ranges in aerosol instrument intercomparisons: a case study for the Atmospheric Tomography Mission, *Atmos. Meas. Tech.*, 14, 3631-3655, doi: 10.5194/amt-14-3631-2021, 2021.
- 1075 Guo, H., Nenes, A., and Weber, R. J.: The underappreciated role of nonvolatile cations in aerosol ammonium-sulfate molar ratios, *Atmos. Chem. Phys.*, 18, 17307-17323, doi: 10.5194/acp-18-17307-2018, 2018.
- 1080 Guo, H., Liu, J., Froyd, K. D., Roberts, J. M., Veres, P. R., Hayes, P. L., Jimenez, J. L., Nenes, A., and Weber, R. J.: Fine particle pH and gas-particle phase partitioning of inorganic species in Pasadena, California, during the 2010 CalNex campaign, *Atmos. Chem. Phys.*, 17, 5703-5719, doi: 10.5194/acp-17-5703-2017, 2017.
- 1085 Guo, H., Weber, R. J., and Nenes, A.: High levels of ammonia do not raise fine particle pH sufficiently to yield nitrogen oxide-dominated sulfate production, *Scientific Reports*, 7(1), <https://doi.org/10.1038/s41598-017-11704-0>, 2017.
- 1090 Guo, H., Xu, L., Bougiatioti, A., Cerully, K. M., Capps, S. L., Hite, J. R., Carlton, A. G., Lee, S.-H., Bergin, M. H., Ng, N. L., Nenes, A., and Weber, R. J.: Fine-particle water and pH in the southeastern United States, *Atmos. Chem. Phys.*, 15, 5211–5228, 2015.
- 1095 Heim, E. W., Dibb, J., Scheuer, E., Jost, P. C., Nault, B. A., Jimenez, J. L., Peterson, D., Knote, C., Fenn, M., Hair, J., Beyersdorf, A. J., Corr, C., and Anderson, B. E.: Asian dust observed during KORUS-AQ facilitates the uptake and incorporation of soluble pollutants during transport to South Korea, *Atmos. Environ.*, 224, doi: 10.1016/j.atmosenv.2020.117305, 2020.
- 1100 Hinckley, E.-L. S., Crawford, J. T., Fakhraei, H., and Driscoll, C. T.: A shift in sulfur-cycle manipulation from atmospheric emissions to agricultural additions, *Nat. Geosci.*, 13, 597–604, <https://doi.org/10.1038/s41561-020-0620-3>, 2020.
- 1105 Hoesly, R. M., Smith, S. J., Feng, L., Klimont, Z., Janssens-Maenhout, G., Pitkanen, T., Seibert, J. J., Vu, L., Andres, R. J., Bolt, R. M., Bond, T. C., Dawidowski, L., Kholod, N., Kurokawa, J.-I., Li, M., Liu, L., Lu, Z., Moura, M. C. P., O'Rourke, P. R., and Zhang, Q.: Historical (1750–2014) anthropogenic emissions of reactive gases and aerosols from the Community Emissions Data System (CEDS), *Geosci. Model Dev.*, 11, 369-408, <https://doi.org/10.5194/gmd-11-369-2018>, 2018.

- 1110 Keresztesi, A., Nita, I.-A., Boga, R., Birsan, M.-V., Bodor, Z., Szep, R.: Spatial and long-term analysis of rainwater chemistry over the conterminous United States, *Environ. Res.* 188, 109872, <https://doi.org/10.1016/j.envres.2020.109872>, 2020.
- 1115 Koch, D., Jacob, D., Tegen, I., Rind, D., and Chin, M.: Tropospheric sulfur simulation and sulfate direct radiative forcing in the Goddard Institute for Space Studies general circulation model, *J. Geophys. Res.*, 104 (D19), 23,799-23,822, <https://doi.org/10.1029/1999JD900248>, 1999.
- 1120 Kreidenweis, S. M., Petters, M. D., and De Mott, P. J.: Single-parameter estimates of aerosol water content, <https://doi.org/10.1088/1748-9326/3/3/035002>, 2008.
- 1125 Lee, C., Martin, R. V., van Donkelaar, A., Lee, H., Dickerson, R. R., Hains, J. C., Krotkov, N., Richter, A., Vinnikov, K., and Schwab, J. J.: SO₂ emissions and lifetimes: Estimates from inverse modeling using in situ and global, space-based (SCIAMACHY and OMI) observations, *J. Geophys. Res.*, 116(D06304), 1-13, doi:10.1029/2010JD014758, 2011.
- 1130 Lewis, K. A., Arnott, W. P., Moosmüller, H., Chakrabarty, R. K., Carrico, C. M., Kreidenweis, S. M., Day, D. E., Malm, W. C., Laskin, A., Jimenez, J. L., Ulbrich, I. M., Huffman, J. A., Onasch, T. B., Trimborn, A., Liu, L., and Mishchenko, M. I.: Reduction in biomass burning aerosol light absorption upon humidification: roles of inorganically-induced hygroscopicity, particle collapse, and photoacoustic heat and mass transfer, *Atmos. Chem. Phys.*, 9, 8949–8966, <https://doi.org/10.5194/acp-9-8949-2009>, 2009.
- 1135 Liao, J., Wolfe, G. M., Hannun, R. A., St. Clair, J. M., Hanisco, T. F., Gilman, J. B., Lamplugh, A., Selimovic, V., Diskin, G. S., Nowak, J. B., Halliday, H. S., DiGangi, J. P., Hall, S. R., Ullmann, K., Holmes, C. D., Fite, C. H., Agastra, A., Ryerson, T. B., Peischl, J., Bourgeois, I., Warneke, C., Coggon, M. M., Gkatzelis, G. I., Sekimoto, K., Fried, A., Richter, D., Weibring, P., Apel, E. C., Hornbrook, R. S., Brown, S. S., Womack, C. C., Robinson, M. A., Washenfelder, R. A., Veres, P. R., and Neuman, J. A.: Formaldehyde evolution in US wildfire plumes during the Fire Influence on Regional to Global Environments and Air Quality experiment (FIREX-AQ), *Atmos. Chem. Phys.*, 21, 18319–18331, <https://doi.org/10.5194/acp-21-18319-2021>, 2021.
- 1140 Lobert, J. M., Scharffe, D. H., Hao, W. M., Kuhlbusch, T. A., Seuwen, R., Warneck, P., and Crutzen, P. J.: Experimental evaluation of biomass burning emissions: Nitrogen and carbon containing compounds, in *Global Biomass Burning: Atmospheric, Climatic and Biospheric Implications*, edited by J. S. Levine, pp. 289-304, MIT Press, Cambridge, Mass., 1991.
- 1145 Meng, Z., and Seinfeld, J. H.: Time scales to achieve atmospheric gas-aerosol equilibrium for volatile species, *Atmos. Environ.*, 30, 2889-2900, doi: 10.1016/1352-2310(95)00493-9, 1996.
- 1150 Moch, J. M., Dovrou, E., Mickley, L. J., Keutsch, F. N., Cheng, Y., Jacob, D. J., Jiang, J., Li M., Munger, J. W., Qiao, X., and Zhang, Q.: Contribution of hydroxymethane sulfonate to ambient particulate matter: A potential explanation for high particulate sulfur during severe winter haze in Beijing. *Geophysical Research Letters*, 45, 11,969-11,979, <https://doi.org/10.1029/2018GL079309>, 2018.

- 1155 Müller, M., Anderson, B. E., Beyersdorf, A. J., Crawford, J. H., Diskin, G. S., Eichler, P., Fried, A., Keutsch, F. N., Mikoviny, T., Thornhill, K. L., Walega, J. G., Weinheimer, A. J., Yang, M., Yokelson, R. J., and Wisthaler, A.: In situ measurements and modeling of reactive trace gases in a small biomass burning plume, *Atmos. Chem. Phys.*, 16, 3813–3824, <https://doi.org/10.5194/acp-16-3813-2016>, 2016.
- 1160 National Atmospheric Deposition Program (NRSP-3). NADP Program Office, Wisconsin State Laboratory of Hygiene, 465 Henry Mall, Madison, WI 53706, 2022.
- 1165 Nault, B. A., Campuzano-Jost, P., Day, D. A., Jo, D. S., Schorder, J. C., Allen, H. M., Bahreini, R., Bian, H., Blake, D. R., Chin, M., Clegg, S. L., Colarco, P. R., Crouse, J. D., Cubison, M. J., DeCarlo, P. F., Dibb, J. E., Diskin, G. S., Hodzic, A., Hu, W., Katich, J. M., Kim, M. J., Kodros, J. K., Kupc, A., Lopez-Hilfiker, F. D., Marais, E. A., Middlebrook, A. M., Neuman, J. A., Nowak, J. B., Palm, B. B., Paulot, F., Pierce, J. R., Schill, G. P., Scheuer, E., Thornton, J. A., Tsigaridis, K., Wennberg, P. O., Williamson, C. J., and Jimenez J. L.: Chemical transport models often underestimate inorganic aerosol acidity in remote regions of the atmosphere. *Commun Earth Environ* 2, 93, <https://doi.org/10.1038/s43247-021-00164-0>, 2021.
- 1170 Paatero, P. and Tapper, U.: Positive Matrix Factorization: a non-negative factor model with optimal utilization of error estimates of data values, 5, 111–126, <https://doi.org/10.1002/env.3170050203>, 1994.
- 1175 Pandis, S. N., Wexler, A. S., and Seinfeld, J. H.: Dynamics of Tropospheric Aerosols, *J. Phys. Chem.*, 99 9646-9659, <https://doi.org/10.1021/j100024a003>, 1995.
- 1180 Pattantyus, A. K., Businger, S., and Howell, S. G.: Review of sulfur dioxide to sulfate aerosol chemistry at Kilauea Volcano, Hawai'i, *Atm. Env.*, 185, 262-271, <https://doi.org/10.1016/j.atmosenv.2018.04.055>, 2018.
- 1185 Pham, M., J.-F. Muller, G. P. Brasseur, C. Granier, and G. Megie, A three-dimensional study of the tropospheric sulfur cycle, *J. Geophys. Res.*, 100, 26,061-26,092, <https://doi.org/10.1029/95JD02095>, 1995.
- 1190 Pilinis, C., Seinfeld, J. H., and Grosjean, D.: Water content of atmospheric aerosols, *Atmos. Environ.* (1967), 23, 1601-1606, doi: 10.1016/0004-6981(89)90419-8, 1989.
- 1190 Qu, R. and Han, G.: A critical review of the variation in rainwater acidity in 24 Chinese cities during 1982–2018, *Elem. Sci. Anth.*, 9(1), <https://doi.org/10.1525/elementa.2021.00142>, 2021.
- 1195 Rickly, P. S., Xu, L., Crouse, J. D., Wennberg, P. O., and Rollins, A. W.: Improvements to a laser-induced fluorescence instrument for measuring SO₂ – impact on accuracy and precision, *Atmos. Meas. Tech.*, 14, 2429–2439, <https://doi.org/10.5194/amt-14-2429-2021>, 2021.
- Sachse, G. W., Jr, J. E. C., Hill, G. F., Wade, L. O., Burney, L. G., and Ritter, J. A.: Airborne tunable diode laser sensor for high-precision concentration and flux measurements of carbon

- 1200 monoxide and methane, in: Measurement of Atmospheric Gases, Measurement of Atmospheric
Gases, 157–166, <https://doi.org/10.1117/12.46162>, 1991.
- 1205 [Scheuer, E., Talbot, R. W., Dibb, J. E., Seid, G. K. & DeBell, L. Seasonal distributions of fine
aerosol sulfate in the North American Arctic basin during TOPSE. *J. Geophys. Res.* 108, 643,
2003.](#)
- Schueneman, M. K., Nault, B. A., Campuzano-Jost, P., Jo, D. S., Day, D. A., Schroder, J. C.,
Palm, B. B., Hodzic, A., Dibb, J. E., and Jimenez, J. L.: Aerosol pH indicator and organosulfate
1210 detectability from aerosol mass spectrometry measurements, *Atmos. Meas. Tech.*, 14, 2237–
2260, <https://doi.org/10.5194/amt-14-2237-2021>, 2021.
- Seinfeld, J. H., and Pandis, S. N.: *Atmospheric Chemistry and Physics: From Air Pollution and
Climate Change*, John Wiley, New York, 2006.
- 1215 Shao, J., Chen, Q., Wang, Y., Lu, X., He, P., Sun, Y., Shah, V., Martin, R. V., Philip, S., Song,
S., Zhao, Y., Xie, Z., Zhang, L., and Alexander, B.: Heterogeneous sulfate aerosol formation
mechanisms during wintertime Chinese haze events: air quality model assessment using
observations of sulfate oxygen isotopes in Beijing, *Atmos. Chem. Phys.*, 19, 6107–6123,
1220 <https://doi.org/10.5194/acp-19-6107-2019>, 2019.
- [Shingler, T. et al. Airborne Characterization of Sub-saturated Aerosol Hygroscopicity and Dry
Refractive Index from the Surface to 6.5 km during the SEAC4RS Campaign. *J. Geophys. Res.*
D: Atmos. 121, 4188–4210, 2016.](#)
- 1225 Sinha, P., Hobbs, P. V., Yokelson, R. J., Bertschi, I. T., Blake, D. R., Simpson, I. J., Gao, S.,
Kirchstetter, T. W., and T. Novakov, T.: Emissions of trace gases and particles from savanna
fires in southern Africa, *J. Geophys. Res.*, 108(D13), 8487, doi:10.1029/2002JD002325, 2003.
- 1230 Smith, S. J., van Aardenne, J., Klimont, Z., Andres, R. J., Volke, A., and Delgado Arias, S.:
Anthropogenic sulfur dioxide emissions: 1850–2005, *Atmos. Chem. Phys.*, 11, 1101–1116,
<https://doi.org/10.5194/acp-11-1101-2011>, 2011.
- 1235 Solberg, E. D., Malhi, S. S., Nyborg, M., Gill, K. S.: Fertilizer Type, Tillage, and Application
Time Effects on Recovery of Sulfate-S from Elemental Sulfur Fertilizers in Fallow Field Soils,
Communications in Soil Science and Plant Analysis, 34(5-6), 815-830,
<https://doi.org/10.1081/CSS-120018977>, 2011.
- 1240 Song, S., Ma, T., Zhang, Y., Shen, L., Liu, P., Li, K., Zhai, S., Zheng, H., Gao, M., Moch, J. M.,
Duan, F., He, K., and McElroy, M. B.: Global modeling of heterogeneous
hydroxymethanesulfonate chemistry, *Atmos. Chem. Phys.*, 21, 457–481,
<https://doi.org/10.5194/acp-21-457-2021>, 2021.
- Sullivan, R. C., Boyer-Chelmo, H., Gorkowski, K., and Beydoun, H.: Aerosol Optical Tweezers
Elucidate the Chemistry, Acidity, Phase Separations, and Morphology of Atmospheric

- 1245 Microdroplets, *Acc. Chem. Res.*, 53(11), 2498–2509, <https://doi.org/10.1021/acs.accounts.0c00407>, 2020.
- Susott, R. A., Olbu, G. J., Baker, S. P., Ward, D. E., Kauffmann, J. B., and Shea, R. W.: Carbon, hydrogen, nitrogen, and thermogravimetric analysis of tropical ecosystem biomass, in *Biomass Burning and Global Change*, vol. 1, edited by J. S. Levine, pp. 249 – 259, MIT Press, Cambridge, Mass., 1996.
- 1250
- Tang, M. J., Telford, P. J., Pope, F. D., Rkiouak, L., Abraham, N. L., Archibald, A. T., Braesicke, P., Pyle, J. A., McGregor, J., Watson, I. M., Cox, R. A., and Kalberer, M.: Heterogeneous reaction of N₂O₅ with airborne TiO₂ particles and its implication for stratospheric particle injection, *Atmos. Chem. Phys.*, 14, 6035–6048, <https://doi.org/10.5194/acp-14-6035-2014>, 2014.
- 1255
- Ulbrich, I. M., Canagaratna, M. R., Zhang, Q., Worsnop, D. R., and Jimenez, J. L.: Interpretation of organic components from Positive Matrix Factorization of aerosol mass spectrometric data, *Atmos. Chem. Phys.*, 9, 2891–2918, 2009.
- 1260
- U.S. Department of Agriculture: Crop Production 2019 Summary. By S. L. Censky and J. L. Parsons. January 2020. ISSN: 1057-7823, 2020.
- 1265
- [van Donkelaar, A., Martin, R. V., Leaitch, W. R., Macdonald, A. M., Walker, T. W., Streets, D. G., Zhang, Q., Dunlea, E. J., Jimenez, J. L., Dibb, J. E., Huey, L. G., Weber, R., and Andreae, M. O.: Analysis of aircraft and satellite measurements from the Intercontinental Chemical Transport Experiment \(INTEX-B\) to quantify long-range transport of East Asian sulfur to Canada, *Atmos. Chem. Phys.*, 8, 2999-3014, doi: 10.5194/acp-8-2999-2008, 2008.](#)
- 1270
- Vay, S. A., Tyler, S. C., Choi, Y., Blake, D. R., Blake, N. J., Sachse, G. W., Diskin, G. S., and Singh, H. B.: Sources and transport of $\Delta^{14}\text{C}$ in CO₂ within the Mexico City Basin and vicinity, *Atmos. Chem. Phys.*, 9, 4973–4985, <https://doi.org/10.5194/acp-9-4973-2009>, 2009.
- 1275
- Wang, G., Zhang, R., Gomez, M. E., Yang, L., Zamora, M. L., Hu, M., Lin, Y., Peng, J., Guo, S., Meng, J., Li, J., Cheng, C., Hu, T., Ren, Y., Wang, Y., Gao, J., Cao, J., An, Z., Zhou, W., Li, G., Wang, J., Tian, P., Marrero-Ortiz, W., Secret, J., Du, Z., Zheng, J., Shang, D., Zeng, L., Shao, M., Wang, W., Huang, Y., Wang, Y., Zhu, Y., Li, Y., Hu, J., Pan, B., Cai, L., Cheng, Y., Ji, Y., Zhang, F., Rosenfeld, D., Liss, P. S., Duce, R. A., Kolb, C. E., and Molina, M. J.: Persistent sulfate formation from London Fog to Chinese haze, *PNAS*, 113(48), 13630-13635, <https://doi.org/10.1073/pnas.1616540113>, 2016.
- 1280
- Wang, Y., Zhang, Q. Q., Jiang, J., Zhou, W., Wang, B., He, K., Duan, F., Zhang, Q., Philip, S., and Xie, Y.: Enhanced sulfate formation during China's severe winter haze episode in January 2013 missing from current models, *J. Geophys. Res. Atmos.*, 119, 10,425–10,440, 2014, doi:10.1002/2013JD021426, 2014.
- 1285

- 1290 Westerling, A. L., Hidalgo, H. G., Cayan, D. R., and Swetnam, T. W.: Warming and Earlier
Spring Increase Western U.S. Forest Wildfire Activity, *Science*, 313(5789), 940-943,
<https://doi.org/10.1126/science.1128834>, 2006.
- 1295 Wolfe, G. M., Marvin, M. R., Roberts, S. J., Travis, K. R., and Liao, J.: The framework for 0-D
atmospheric modeling (F0AM) v3.1, *Geosci. Model Dev.*, 9(9), 3309-3319. DOI:10.5194/gmd-
9-3309-2016, 2016.
- 1300 Yokelson, R. J., Griffith, D. W., and Ward, D. E.: Open-path Fourier transform infrared studies
of large-scale laboratory biomass fires, *Geophys. Res. Atmos.*, 101(D15), 21067-21080,
<https://doi.org/10.1029/96JD01800>, 1996.
- Zhang, Q., Zhou, S., Collier, S., Jaffe, D., Onasch, T., Shilling, J., Kleinman, L., and Sedlacek,
A.: Understanding Composition, Formation, and Aging of Organic Aerosols in Wildfire
Emissions via Combined Mountain Top and Airborne Measurements. *ACS Symposium Series*,
1299, Chapter 18, 363-385, <https://doi.org/10.1021/bk-2018-1299.ch018>, 2018.